Journal of Oceanography, Vol. 58, pp. 403 to 420, 2002

Cross-Frontal Water Exchange on Georges Bank: Some Results from an U.S. GLOBEC/Georges Bank Program Model Study

CHANGSHENG CHEN[1]* and ROBERT C. BEARDSLEY[2]

[1]*School for Marine Science and Technology, University of Massachusetts-Dartmouth, 706 South Rodney French Boulevard, New Bedford, MA 02744-1221, U.S.A.*
[2]*Department of Physical Oceanography, Woods Hole Oceanographic Institution, Woods Hole, MA 02543, U.S.A.*

(Received 28 February 2001; in revised form 6 September 2001; accepted 6 September 2001)

This paper reviews recent progress on modeling cross-frontal water exchange on Georges Bank undertaken as part the U.S. Global Ecosystem Northwest Atlantic/ Georges Bank Study (U.S. GLOBEC/Georges Bank Program). A simple conceptual model is described first, followed by a discussion of four physical mechanisms associated with (1) strong nonlinear interaction, (2) asymmetric tidal mixing, (3) varying wind forcing, and (4) chaotic mixing. Some critical issues in modeling studies of fronts are also addressed. A new unstructured grid, finite-volume coastal ocean ecosystem model is introduced. This model combines the best of the finite-difference method for the simplest discrete computational efficiency and the finite-element method for geometric flexibility. Because the finite-volume method discretizes the integral form of the governing equations, this approach provides a better representation for the conservation laws of mass and momentum are satisfied, which is particularly important in the frontal regions.

Keywords:
· Numerical modeling,
· frontal dynamics,
· ecosystem,
· tidal mixing,
· finite volume model.

1. Introduction

Georges Bank (GB) is a shallow submarine bank on the southern edge of the Gulf of Maine (Fig. 1). GB is separated from Nantucket Shoals to the west by the Great South Channel and from the Scotian Shelf to the east by the Northeast Channel. In plane view, GB is roughly elliptical, with a length of about 200 km and a width of about 150 km. From south to north, the cross-bank bottom topography rises steeply with a slope of about 0.01 from 1000 m on the upper slope to 100 m at the shelf break, then increases slowly with a slope of roughly 0.001 to 40 m over a distance of about 75 km towards the crest of the bank, and then decreases rapidly with a slope of about 0.03 to a depth of 300 m in the deep basin just north of the bank crest.

Flow over GB is dominated by strong M_2 tidal currents. These currents exhibit a rotary character over the bank and increase as the water becomes shallower. The maximum velocity is about 30 cm/s near the shelf break on the southern flank and about 100 cm/s at the edge of the northern flank (Moody *et al*., 1984). When a long barotropic tidal wave propagates from the deep ocean onto variable bottom topography, a clockwise-rectified flow is generated over the bank due to the nonlinear transfer of vorticity and momentum from tidal currents (Zimmerman, 1978, 1980; Loder, 1980; Greenberg, 1983). This tidal rectified topographically current moves eastward as a current jet of about 20 cm/s on the northern flank and re-circulates westward as a relatively broad and weaker flow of 1–3 cm/s on the southern flank. Whenever stratification is involved, strong tidal-induced vertical mixing creates a well-defined tidally mixed front (TMF) around the shallow cap of the Bank. During summer, the TMF is located near the 40-m isobath on the northern flank and about the 50 to 60-m isobath on the southern flank (Flagg, 1987; Chen *et al*., 1995a). During winter, the TMF disappears over the southern flank as strong wind mixing and surface cooling homogenize the local water column on the top and flanks of the Bank (Fig. 2). Because of the TMF, the clockwise re-circulation gyre over GB varies significantly with seasons, strongest during the summer in which the maximum along-bank current can reach 30 to 40 cm s^{-1} on the northern flank, and about 8 to 10 cm s^{-1} on the southern flank, and weakest

* Corresponding author. E-mail: c1chen@UMassD.Edu

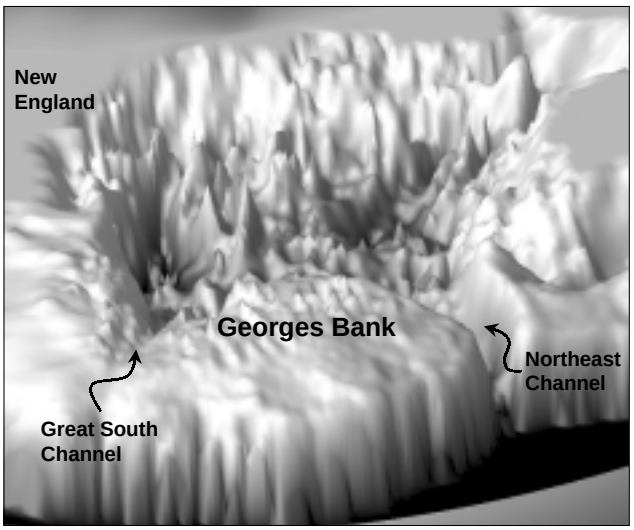

Fig. 1. Bathymetry of the New England, Gulf of Maine/Georges Bank.

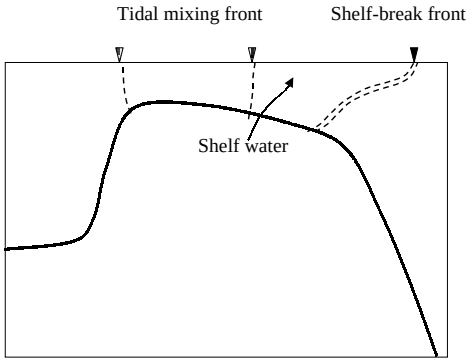

Fig. 2. A 2-D illustration of tidal mixing and shelfbreak fronts on Georges Bank.

during the winter when the very weak tidally driven rectified residual currents are in competition with wind- and buoyancy-driven flow (Butman *et al*., 1982; Loder and Wright, 1985; Chen *et al*., 1995a; Limeburner and Beardsley, 1996).

The unique physical processes of the clockwise residual circulation gyre, tidal mixing, and tidal mixing front on GB make it one of the most productive shelf ecosystem in the world (Riley, 1941; O'Reilly *et al*., 1987; Horne *et al*., 1989; Wiebe and Beardsley, 1996; Franks and Chen, 1996, 2001). The total annual production on the bank is two-to-three times higher than the mean value of the annual production over continental shelves in the world. Patterns of high plankton patchiness are often recorded on GB, with an unusually high concentration of chlorophyll in the vertically well-mixed region and frontal zone (O'Reilly *et al*., 1987; Horne *et al*., 1989; Mountain and Taylor, 1996). Cod and haddock spawn on the northeast flank of GB in late winter and early spring (Smith and Morse, 1985). Their eggs and young larvae move following the clockwise residual circulation gyre and arrive on the southern flank in late April and May, with a high abundance of cod and haddock larvae found in the stratified region between tidal and shelf break fronts on the southern flank (Lough, 1984; Townsend and Pettigrew, 1996; Lough and Mountain, 1996). These larval fishes continue to move westward and northeastward following the recirculation and grow to pelagic juveniles on the western flank in late spring. Demersal juveniles occupy the mixed region on GB in early summer, suggesting a significant cross-frontal onbank transport on GB (Lough and Manning, 2001) (Fig. 3).

The U.S. Global Ecosystem Northwest Atlantic/Georges Bank Study (U.S. GLOBEC/Georges Bank Program) is a multi-year interdisciplinary program with objectives of "understanding the population dynamics of four key species on the Bank-cod, haddock, and the zooplankton *Calanus finmarchicus* and *Pseudocalanus* in terms of their coupling to the physical environment and in terms of their predators and prey. The ultimate goal is to be able to predict changes in the distribution and abundance of these species as a result of changes in their physical and biotic environment as well as to anticipate how their populations might respond to climate change" (U.S. GLOBEC, 1992). This program includes a multi-year efforts with several phases. The pilot study started in 1992, and the main field program began in late 1994. Phase I field work (1995–96) focused on process studies on the effects of stratification on the target species, phase II (1997–98) examined sources, retention, and losses of the target species on the Bank, and phase III (1999–2000) investigated in detail frontal-exchange processes.

In this paper, we review progress made in model studies of cross-frontal-exchange processes on Georges Bank conducted as part of the U.S. GLOBEC/Georges Bank Program phase III study. The remaining sections are organized as follows. In Section 2, a conceptual model of tidal and density fronts is described. In Section 3, four physical mechanisms for cross-frontal water exchange are discussed, and in Section 4, some critical issues in modeling studies are addressed and a new model approach is introduced. Finally, a summary is given in Section 5. Since this is still an ongoing program, our review given here will not cover all aspects of the phase III work, especially the field measurements. Updates on phase III work can be tracked on the U.S. GLOBEC/Georges Bank Program web site: http://globec.whoi.edu/globec-dir, and recent results of our modeling efforts can be viewed on our web site: http://rfac.smast.umassd.edu/MEDM/

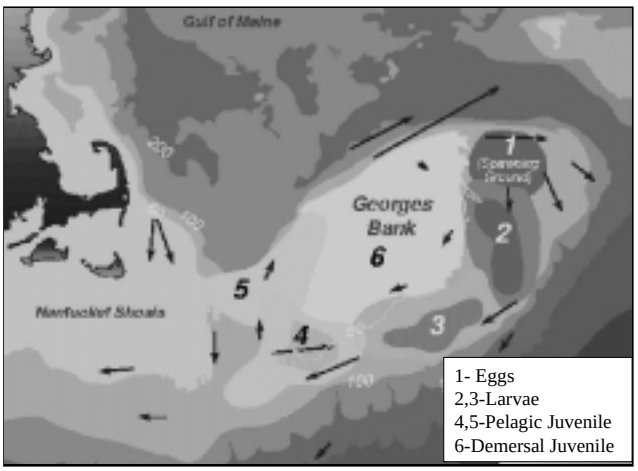

Fig. 3. The diagram showing the motion of a larval fish patch during the first six months from spawning. Vectors are the residual currents measured from the long-term moored current meters. This diagram was provided by the U.S. GLOBEC/Georges Bank Program office, which was originally drawn by Lough *et al*. (1985).

2. A Semi-Analytical Diagnostic Model of the Coastal Front

The structure of the frontal circulation is controlled by complex physical processes associated with tidal mixing and density gradients. In a quasi-linear, two-dimensional (2D) system where nonlinear advection and along-front variation can be ignored, the steady current at a density front satisfy the following equations:

$$-fv = -g\frac{\partial \zeta}{\partial x} - \frac{g}{\rho_o}\frac{\partial}{\partial x}\int_z^0 \rho dz + \frac{\partial}{\partial z}\left(K_m \frac{\partial u}{\partial z}\right), \tag{1}$$

$$fu = \frac{\partial}{\partial z}\left(K_m \frac{\partial v}{\partial z}\right), \tag{2}$$

$$\frac{\partial u}{\partial x} + \frac{\partial w}{\partial z} = 0. \tag{3}$$

Given a front-like density field in the form of

$$\rho = \begin{cases} \rho_o - 1000 + \dfrac{\Delta\rho}{2}\left(s - \cos\dfrac{\pi z}{h_o}\right) & x \le 0 \\ \rho_o - 1000 + \dfrac{\Delta\rho}{2}\left(1 - \dfrac{x}{L}\right)\left[s - \cos\dfrac{\pi z}{h(x)}\right] & 0 < x \le L \\ \rho_o - 1000 & x > L, \end{cases} \tag{4}$$

where ρ_o, $\Delta\rho$, and $h(x) = h_o - \alpha x$ are the mean density, density difference, and water depth, respectively. s is a parameter that controls the distribution of density. The mixing coefficient is specified as

$$K_m = \frac{u_*^2}{200 f}\left(1 + 7\overline{R_i}\right)^{-\frac{1}{4}} \tag{5}$$

where $u_* = \sqrt{C_D}\overline{U}$, $\overline{R_i} = g(\Delta\rho/\rho_o)h(x)/\overline{U}^2$, and f, C_D, and $\overline{U}$ are the Coriolis parameter, bottom drag coefficient, and the r.m.s. tidal current.

Garrett and Loder (1981) diagnostically calculated the along- and cross-frontal current using Eqs. (1)–(3). If $\Delta\rho$ is constant, $\overline{R_i}$ is independent of z. Therefore we can analytically solve these equations for a given density distribution (4) and mixing coefficient (5). The solution is

$$u = e^{\frac{z}{\delta E}}\left(C_1 \cos\frac{z}{\delta E} - C_2 \sin\frac{z}{\delta E}\right) + e^{-\frac{z}{\delta E}}\left(C_3 \cos\frac{z}{\delta E} + C_4 \sin\frac{z}{\delta E}\right) \tag{6}$$

$$v = e^{\frac{z}{\delta E}}\left(C_1 \sin\frac{z}{\delta E} + C_2 \cos\frac{z}{\delta E}\right) + e^{-\frac{z}{\delta E}}\left(-C_3 \sin\frac{z}{\delta E} + C_4 \cos\frac{z}{\delta E}\right) + \frac{g}{f\rho_o}\int_z^0 \frac{\partial \rho}{\partial x} dz \tag{7}$$

where $\delta E = \sqrt{2K_m / f}$ is the Ekman thickness. C_1, C_2, C_3 and C_4 are the coefficients that can be determined by the boundary conditions at the sea surface ($\partial u/\partial z = \partial v/\partial z = 0$: no wind stress) and at the bottom ($\partial v/\partial z = 0$ and $v = 0$: zero net cross-isobath volume flux). Since K_m and ρ are functions of x, these four coefficients are dependent on x. They must be determined by solving a linear algebra equation with four unknown variables for a given x location.

For given parameters $s = 0.5$, $\overline{U} = 0.5$ m s^{-1}, $f = 10^{-4}$ s^{-1}, $C_D = 2.5 \times 10^{-3}$, $\rho_o = 1025$ kg m^{-3}, $\alpha = 0.0007$, $h_o = 95$ m, and $L = 70$ km, we have used Eqs. (6) and (7) and the above boundary conditions to calculate the along- and cross-frontal currents; the resulting density and current distributions are shown in Fig. 4. In the along-frontal direction, the current is characterized by a relatively strong current jet, with stratified region on the left (facing in the direction of the current on the northern hemisphere) and a maximum speed at a depth of 45 m below the surface, while in the cross-frontal direction, the current consists of double secondary circulation cells with convergence toward the front near the surface and bot-

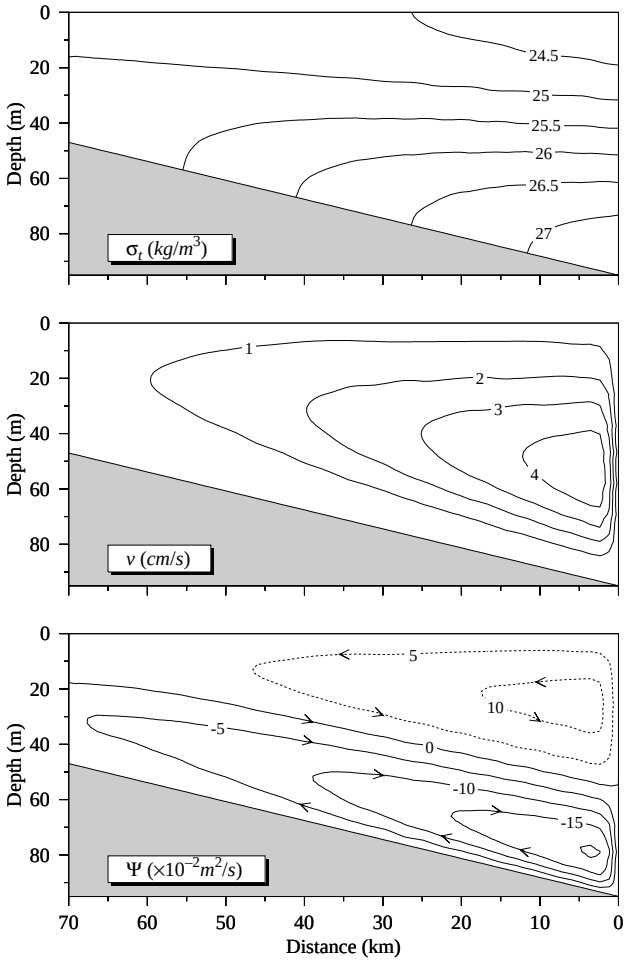

Fig. 4. Distributions of density, along-isobath current and cross-isobath streamfunction calculated using the semi-analytical, diagnostic frontal model.

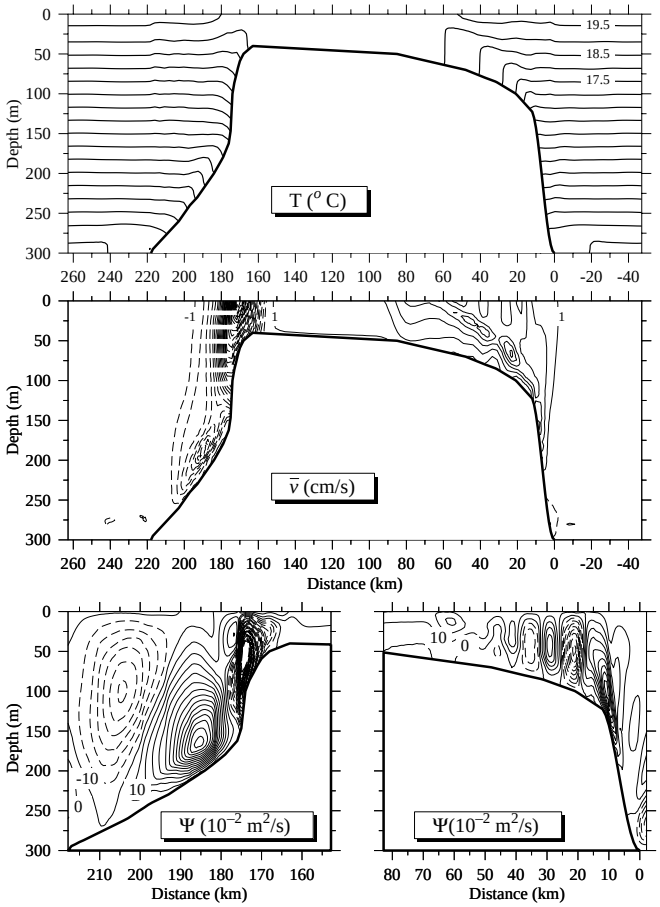

Fig. 5. Cross-bank distributions of tidally-averaged temperature, along-bank velocity, and cross-bank streamfunction. The direction of the along-bank residual current (middle panel): positive-out of the page; negative: into the page. The direction of the cross-bank residual current (lower panel) is defined as $\bar{u} = -\partial\Psi/\partial z$; $\bar{w} = \partial\Psi/\partial x$.

tom. A return flow is found at a subsurface depth along an intermediate density where the density contours split upward and downward.

In this diagnostic case, the structure of the frontal circulation is controlled primarily by two critical parameters: the Ekman number (K_m/fh^2) and s (Garrett and Loder, 1981). Although the distribution of currents could differ significantly in cases with different tidal mixing intensities, distributions of density, and the inclusion of internal tidal interactions, this simple model provides us with a general property of TMF in coastal regions where mixing is dynamically important. When time- and spatial-dependent mixing is taken into account, it may produce multiple secondary circulation cells within the frontal zone over the sloping bottom topography (Chen and Beardsley, 1995; Chen *et al.*, 1995a, 2001a), and these double circulation cells may feature convergence towards the front at the bottom and divergence from the front at the surface (Chapman and Lentz, 1994; Chen and Beardsley, 1998) (Fig. 5).

The frontal zone acts as a retention zone or a dynamic barrier to the cross-shelf exchange of water, dissolved and particulate materials. With no extra forcing, the water tends to move following the secondary circulation cells, so that no cross-frontal net flux could exist. Theoretically speaking, no phytoplankton bloom could occur (or at least could not last for weeks or months) on the top of the bank during summer since there is no continuous nutrient supply to the mixed region due to the existence of tidal mixing front. The fact that the high concentration of chlorophyll-*a* is observed in the mixed region on GB in summer suggests that there should be a significant cross-frontal nutrient transport on the bank (Franks and Chen, 2001). Moreover, the high abundance of copepods and other dominant zooplankton species ob-

served within tidal mixing frontal zone or sometimes in mixed region on the top of GB in summer is believed to be linked with the physical processes associated with the cross-frontal water movement (Lough and Manning, 2001).

Physical mechanisms by which dissolved inorganic nutrients can be transferred across the TMF are all related to the temporal and spatial variations of the front driven by time-dependent external forcings (such as the strong nonlinear interaction of tidal currents over varying bottom topography, asymmetric tidal mixing, time-varying wind stress, periodic tidal oscillations, and the occurrence of baroclinic eddies at the frontal boundary). On GB, the tidally averaged circulation is controlled by tidal rectification processes associated with strong nonlinearity and stratification (Loder, 1980; Chen *et al*., 1995a). The Lagrangian residual flow (the residual velocity of a fluid parcel) differs significantly from the Eulerian residual flow (averaged over a tidal cycle at a fix location), and they oppose each other on the northern flank where the bottom topography is steep (Chen and Beardsley, 1998; Chen *et al*., 2001b). A significant cross-frontal dissolved inorganic nutrient flux could occur due to a strong on-bank Stokes' drift velocity near the bottom (Loder *et al*., 1997; Chen and Beardsley, 1998; Chen *et al*., 2001b).

Tidal mixing exhibits temporal and spatial asymmetries on the southern and northern flanks of GB (Chen and Beardsley, 1998). It is strongest near the bottom around maximum on-bank tidal flow as a result of gravitational instability when denser water is advected upslope over lighter water. Asymmetry of mixing intensity in the flood and ebb tidal currents tends to produce a cross-frontal net flux directed from the stratified region to the mixed region. This flux may account for a portion of cross-frontal inorganic nutrient flux on GB, especially during summer (Pringle and Franks, 2001).

Wind tends to cause a migration of the front toward the direction of the Ekman transport. A significant cross-frontal transfer of particles (fish larvae plankton) could occur due to the variation of the wind stress as a result of combined Ekman advection and mixing (Chen *et al*., 2001c). Moreover, the spring-neap tidal cycle tends to cause fortnightly and monthly oscillations of the location of the TMF. These frontal oscillations act as an external forcing in the nonlinear secondary circulation system, and thus can contribute to cross-frontal chaotic transport (Chen, unpublished manuscript). A significant cross-frontal flux of particles may occur under resonance when the advective time scale (T_{adv}) of the particles is close to the period of the spring-neap tidal cycle.

Eddies often form at the edge of the front as a result of baroclinic instability (Pingree, 1979; Garrett and Loder, 1981). Detachment of these eddies from the TMF tends to intermittently produce a cross-frontal nutrient flux from the stratified region to the mixed region. A description of the role of baroclinic eddies in the cross-frontal water transfer was given in Garrett and Loder (1981).

Here we will focus our discussions on the physical processes associated with nonlinear tidal interaction, asymmetric tidal mixing, varying wind stress and mixing, and the spring-neap tidal oscillation. Again, the U.S. GLOBEC/Georges Bank Program is a large on-going interdisciplinary research program, and the material presented in this paper represent just part of the overall modeling effort undertaken in this program.

3. Physical Processes Controlling Cross-Frontal Transport

3.1 Nonlinear tidal interaction

We used a 3D primitive equation ocean circulation model (ECOM-si) to examine the summertime Lagrangian residual flow on GB (Chen *et al*., 2001b). The model is driven by the M_2 tide and wind stress with an initial condition of the July–August climatologically averaged temperature and salinity fields. The residual Lagrangian velocity $\vec{V}_L$ is defined as

$$\vec{V}_L = \frac{\vec{X}_T - \vec{X}_0}{T} \tag{8}$$

where T is the M_2 tidal period, $\vec{X}_T$ and $\vec{X}_0$ are the end and start positions of a particle over T, and the Stokes' velocity $\vec{V}_S$ is equal to

$$\vec{V}_S = \vec{V}_L - \vec{V}_E \tag{9}$$

where $\vec{V}_E$ is the Eulerian residual velocity averaged over a tidal cycle at a grid point. To calculate the Lagrangian current, we released fluid particles at each grid point at the beginning of a tidal cycle after the tidal motion reached an equilibrium state and then tracked them over a tidal cycle. These particles were also tracked continuously over one month and the trajectories used to detect evidence of cross-frontal water transport.

The model generates a well-defined TMF around GB, located around the 50–60-m isobath on the southern flank and around the 40-m isobath on the northern flank, and a shelfbreak front located near the 100 m isobath on the southern flank (Fig. 6). Correspondingly, a strong clockwise Eulerian residual circulation is found around the TMF, with a maximum speed of 35–45 cm/s on the northwestern flank, 30–35 cm/s on the northern flank, and 5–10 cm/s on the southern flank (Fig. 7: upper panel). On the southern flank, the residual flow tends to move west-

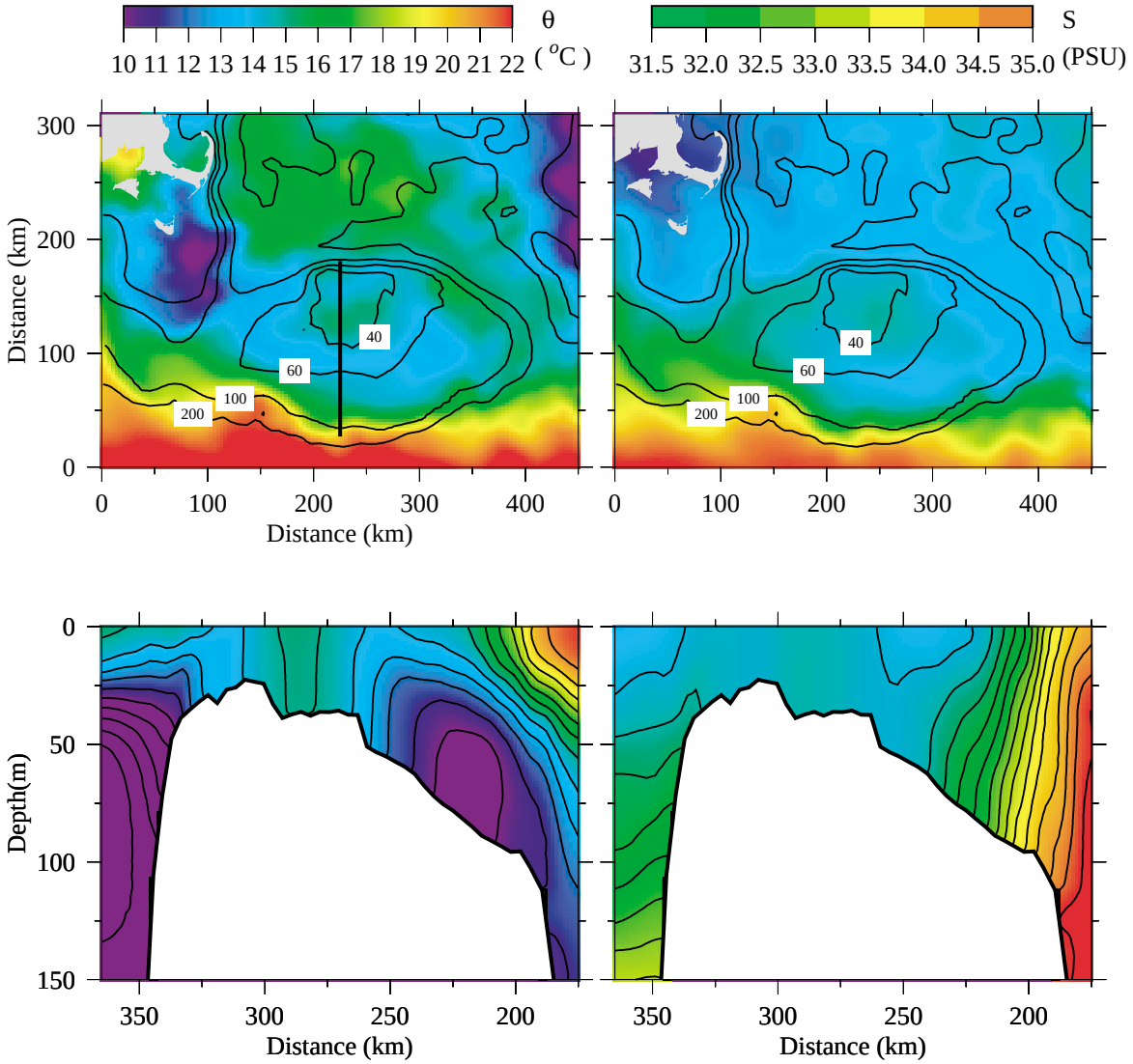

Fig. 6. Distributions of the temperature and salinity near the surface and on a cross-bank section predicted by the prognostic model run with initial conditions using the July-August bimonthly-averaged temperature and salinity fields. The location of the cross-bank section is indicated by a heavy solid line in the upper-left panel.

ward along the local isobaths, with several divergence and convergence zones between tidal and shelf-break fronts. There are clearly convergence currents onbank towards the tidal mixing front at about 50-m isobath and offshore towards the shelfbreak front at about 100-m isobath on the southern flank. The relatively strong westward current found on the southern flank is the result of the summertime intensification of stratification and the onbank flows at the northwestern and northeastern flanks from Brown Bank and Northeast Channel, respectively.

The cross-bank residual current features double circulation cells at the northern edge and multiple circulation cells on the southern flank (Fig. 8: upper panel). On the northern flank, the water tends to converge toward the TMF near the surface, with a strong onbank flow on the deep side and a weak offbank flow on the bank. A strong downwelling exists near the bottom, which tends to be recirculated upward in the upper 150 m off the bank. On the southern flank, the existence of multiple circulation cells between tidal mixing and shelf-break fronts is consistent with the convergence and divergence flow pattern found near the surface. Downwelling also prevails near the bottom of the slope at the shelf break.

The model-predicted Lagrangian residual current differs from the Eulerian residual current in both the horizontal and vertical (Fig. 7: middle panel). At the surface, for example, on the northern and northeastern flanks, the Eulerian current is characterized by significant onbank

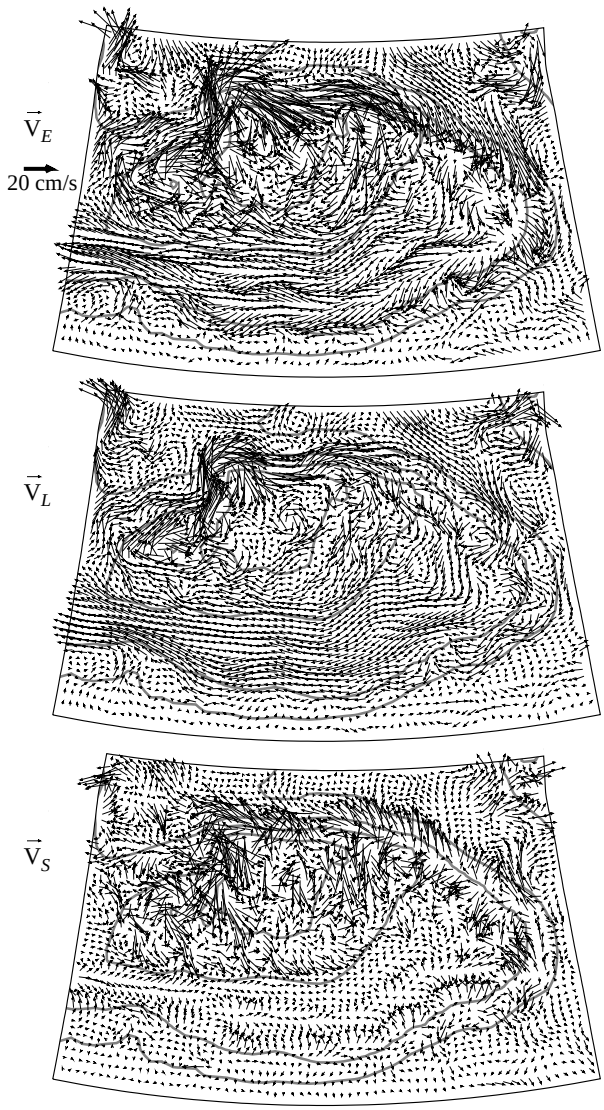

Fig. 7. Distributions of the near-surface residual Eulerian ($\vec{V}_E$), Lagrangian ($\vec{V}_L$), and Stokes' ($\vec{V}_S$) velocities for the case with temperature and salinity fields shown in Fig. 6.

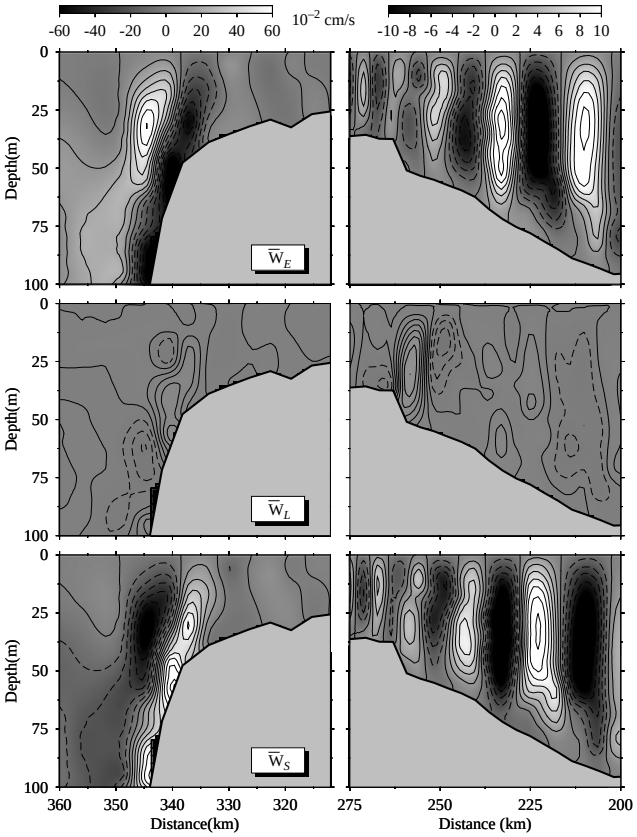

Fig. 8. Cross-bank distributions of the residual Eulerian (W_E), Lagrangian (W_L), and Stokes' (W_S) vertical velocities for the case with temperature and salinity fields shown in Fig. 6.

flow, but the Lagrangian current is almost parallel to the local isobaths. Similar differences also are found on the southern flank, where the Eulerian current shows multiple convergence and divergence zones in the cross-bank direction between tidal mixing and shelf-break fronts, but the Lagrangian current flows mainly along the local isobaths. Around the outer edge of the TMF at the 60-m isobath on the southern flank, the Eulerian current mainly flows along the isobath, but the Lagrangian current converges towards the front.

The disparity in direction and magnitude between residual Lagrangian and Eulerian currents can be viewed clearly on the cross-bank distribution of vertical velocity shown in Fig. 8. On the northern flank, the Lagrangian flow field shows upwelling along the bottom of the slope, which is completely opposite to the downwelling found in the Eulerian flow field. On the southern flank, the vertical residual Lagrangian and Eulerian velocities are opposite around the 50-m isobath where the bottom slope changes sharply. The residual Lagrangian flow field shows strong upwelling around the 50–60-m isobath as a result of the summertime intensification of TMF, and a near-surface convergence zone on the stratified side of TMF. Between the tidal mixing and shelf-break fronts, the Eulerian flow field shows relatively strong multiple secondary circulation cells, but these features almost disappear in the Lagrangian flow field.

The clear difference between Lagrangian and Eulerian currents are caused by the Stokes' drift associated with the bottom slope and stratification (Loder *et al.*, 1997; Chen and Beardsley, 1998; Chen *et al.*, 2001b). On the horizontal plane (Fig. 7: lower panel), the model-predicted Stokes' velocity varies with water depth, larger over the top of GB and on the northwestern, northern and

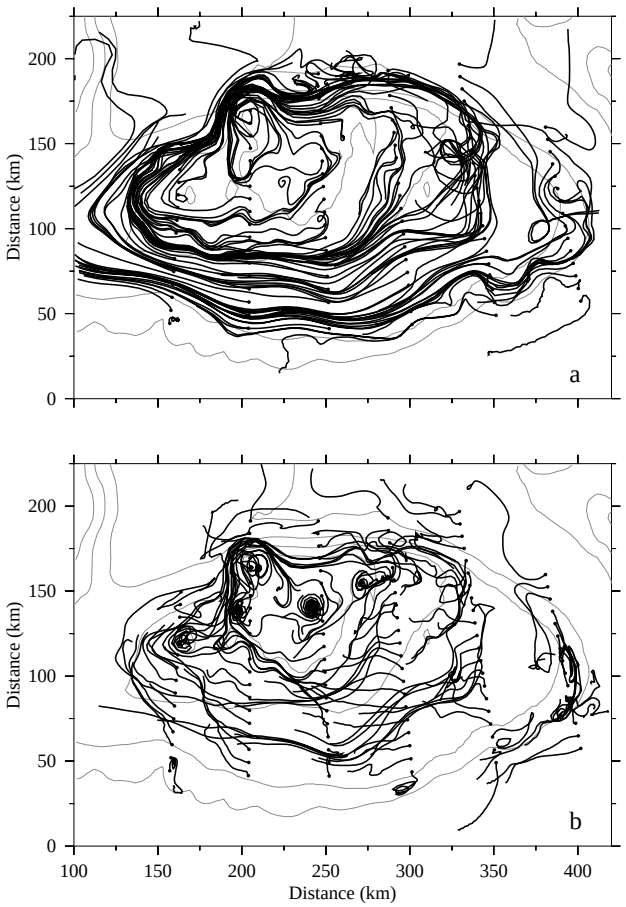

Fig. 9. The near-surface (a) and near-bottom (b) trajectories of particles over Georges Bank for the case with tide only forcing and the temperature and salinity fields shown in Fig. 6. Each dot indicates the initial location of a particle. The particles were released in the July–August stratified flow field at the end of the 10th model day and followed for 30 days.

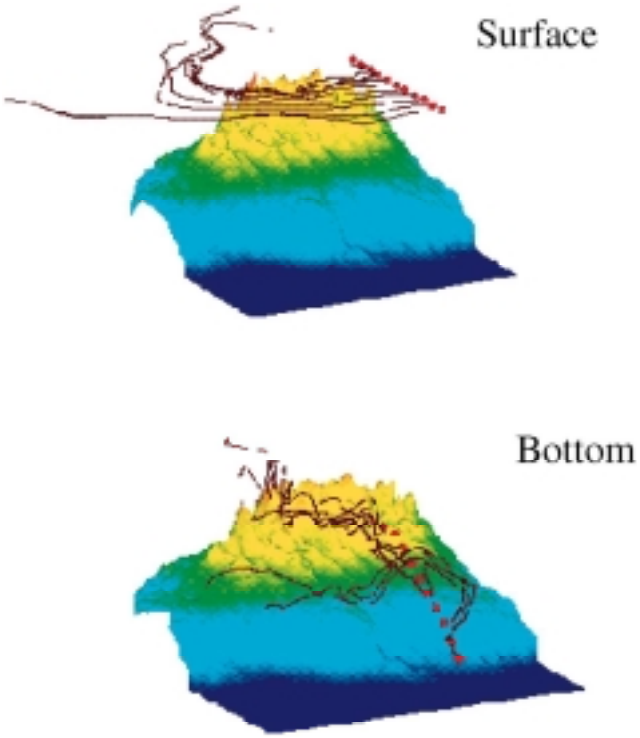

Fig. 10. A 3-D view of selected particle trajectories near the surface and bottom on the southern flank of Georges Bank for the case shown in Fig. 9. The dots show the initial locations of the particles. The particles were tracked for 30 days.

northeastern edges of GB (where tidal currents are strongest or the bottom slope is steep) and smaller in the region deeper than 60 m on the southern flank where the bottom slope changes gradually. On the top of GB, the Lagrange-Euler difference causes a cyclonic Stokes' drift, which is opposite in direction and comparable in magnitude to the Eulerian current. This Stokes' velocity is about 40 to 80% of the Eulerian current and hence significantly reduces the Lagrangian current. On the northeastern flank, the Stokes' velocity is offbank-ward with a comparable speed to the Eulerian velocity. Because of the cancellation between Stokes' and Eulerian currents, the Lagrangian current is mainly parallel to the local isobaths and also is 60 to 70% smaller than the Eulerian current. On the southern flank, between the tidal mixing and shelf-break fronts, the Stokes' velocity field consists of multiple divergence and convergence zones in the cross-bank direction. The cancellation between Stokes' and Eulerian currents causes relatively smooth, along-isobath Lagrangian flow in this area. The Stokes' velocity is relatively smaller near the shelf break because the tidal current is weak and the mean flow is almost dominated by the buoyancy flow associated with the shelf-break front.

In the cross-bank section (Fig. 8: lower panel), the sharp change in the cross-bank tidal flow over the steep bottom topography tends to produce strong nonlinear interaction between tidal currents. This interaction is enhanced in summer, when internal tides are energetic as stratification develops (Chen *et al.*, 1995a). As a result, the vertical component of the Stokes' velocity could be larger than the vertical Eulerian velocity, causing the Lagrangian current to oppose the direction the Eulerian current.

In such a strong nonlinear flow system, the near-surface particles on GB tend to flow clockwise along local isobaths (Fig. 9a), at speeds of 30 to 40 cm/s on the northwestern edge, 25 to 30 cm/s on the northern edge, and 2 to 10 cm/s near the tidal mixing and shelf-break fronts on the southern flank. The clockwise recirculation flows back to the southern flank through three main paths: (1) at the northwestern edge where the bottom topography varies

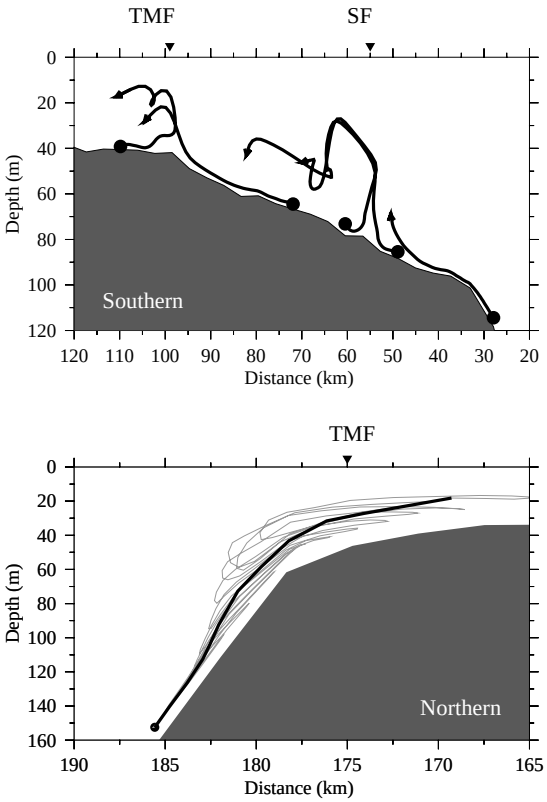

Fig. 11. A 2-D view of selected near-bottom particle trajectories in the cross-bank direction on the southern flank of Georges Bank for the case shown in Fig. 10 (upper panel) and on the northern flank of Georges Bank (lower panel). The heavy solid line indicates the residual trajectory of a particle over tidal cycles, and gray thin solid line in the lower panel indicates the trajectory of a particle at each time step during tidal cycles.

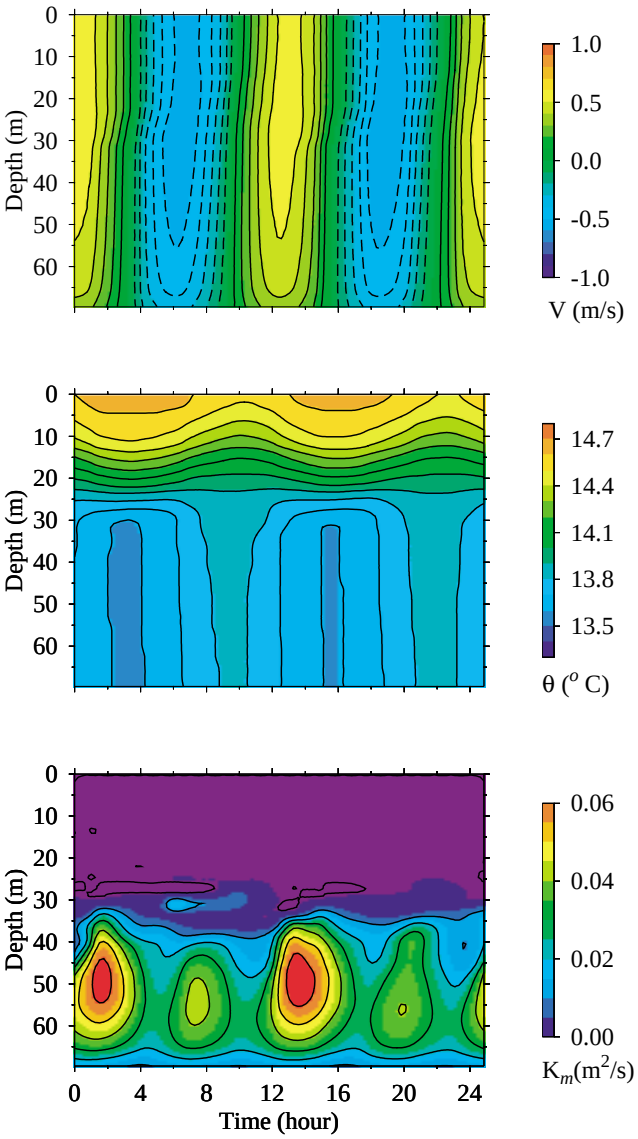

Fig. 12. Model-predicted time series of cross-bank current (V), temperature (θ), vertical thermal and diffusion coefficient (K_m) at a selected site around the 60-m isobath on the center of Georges Bank. This figure is replotted based on figure 16 in Chen *et al*. (2001a).

sharply in both along- and cross-bank directions; (2) between 50- and 60-m isobaths along the tidal mixing front; and (3) along the 100-m isobath at the outer edge of the bank. There is no significant cross-frontal water transport near the surface, except at the northwestern edge where a relatively strong southeastward Lagrangian flow exists.

The near-bottom particle trajectories are generally similar to those observed near the surface, except at the northeastern slope where particles move westward along the bank (Fig. 9b). On the southern flank, a significant frontward convergent flow is found in the center area of the flank, where the near-bottom particles flow northwestward between 60- and 70-m isobaths in the stratified region and southwestard around the 40-m isobath in the mixed region (Figs. 9–11). They meet at the tidal mixing front around the 45- to 50-m isobaths, move upward and then cross the TMF. Another convergence zone is found around the 80-m isobath at the location of the shelf-break front, where the particles around 70-m isobath and at the outer shelf flow towards the front and then move upward to mid-depth at the front (Figs. 10 and 11). This indicates that there is a divergence zone near the bottom between the tidal mixing and shelf-break fronts on the southern flank. On the northern flank, there are remarkable onbank flows. The particles near the bottom flow upward on their along-bank eastward journey and cross the front near the bottom (Fig. 11).

Fluid particle trajectories on GB clearly show evidence of cross-frontal water transport near the bottom.

This is one of the key physical processes for nutrient supply to the mixed region in summer on GB. Physical mechanisms driving this on-bank flux are the on-bank Stokes' drift caused by strong nonlinear interaction of tidal currents on GB (Loder *et al*., 1997; Chen *et al*., 2001b).

3.2 Asymmetric tidal mixing

On GB, particularly in the summer stratified season, tidal mixing generates a bottom boundary layer in the stratified region over varying bottom topography. In this boundary layer, the cross-bank current increases with height from the bottom and reaches its maximum at the top of the layer (Chen *et al*., 1995a; Werner, 1999). In turn, stronger tidal mixing occurs during the flood tide (flowing onbank) as a result of gravitational instability near the bottom (when denser water is advected upslope over lighter water) (Chen and Beardsley, 1998; Pringle and Franks, 2001), leading to an asymmetric character of tidal mixing over a tidal cycle (Fig. 12). This asymmetric tidal mixing could directly cause an onbank, cross-frontal net water flux on GB. This process can be demonstrated using the following simple analytical model.

In the 2D system where the along-isobath variation of all variables is assumed to be zero ($\partial/\partial y = 0$), the *y*-component momentum equation can be rewritten as

$$\frac{\partial V}{\partial t} + fU = -K_m \frac{\partial v}{\partial z}\bigg|_{z=-h(x)} - \frac{\partial}{\partial x}\int_{-h(x)}^{0} uv\,dz \qquad (10)$$

where $U = \int_{-h(x)}^{0} u\,dz$ and $V = \int_{-h(x)}^{0} v\,dz$ are the x and y components of the horizontal transport; u and v are the x and y component of the horizontal velocity; and the definitions of K_m and $h(x)$ are the same as above. In the Cartesian coordinate frame, x increases northward and z increases upward. For simplification, let us assume a linear bottom stress as the form of

$$K_m \frac{\partial v}{\partial z}\bigg|_{z=-h(x)} = k(t)v, \qquad (11)$$

and divide v into tidal (v_T) and residual ($\bar{v}$) parts as

$$v = v_T + \bar{v}, \qquad (12)$$

where $\bar{v}$ satisfies the tidal rectification balance on GB (Loder, 1980) given as

$$\overline{k(t)}\,\bar{v} = \frac{\partial}{\partial x}\int_{-h(x)}^{0} uv\,dz. \qquad (13)$$

Integrating Eq. (10) over a M_2 tidal cycle yields

$$f\bar{U} = -\overline{k(t)v_T} \qquad (14)$$

where $\overline{(\ )} = \int_0^T (\ )dt$ and T is the M_2 tidal period.

On the southern flank of GB, assume that $k(t)$ is a periodic function over a M_2 tidal cycle given as

$$k(t) = \begin{cases} k_f \sin\omega t & 0 \le t \le \pi/\omega \\ -k_e \sin\omega t & \pi/\omega \le t \le 2\pi/\omega \end{cases} \qquad (15)$$

where ω is the frequency of the M_2 tide; k_f and k_e are the maximum mixing coefficients in flood and ebb tides, respectively, with $k_f > k_e$. Let v_T be expressed as

$$v_T = \frac{1}{2}\tilde{v}_T e^{i\omega t} + \frac{1}{2}\tilde{v}_T^* e^{-i\omega t} \qquad (16)$$

where $\tilde{v}_T$ is the complex representation of v_T. Substituting Eqs. (15) and (16) into Eq. (14) yields

$$\bar{U} = \frac{\pi i}{4\omega f}\left(\tilde{v}_T - \tilde{v}_T^*\right)\left(k_e - k_f\right). \qquad (17)$$

Substitution of $\tilde{v}_T = V_R + V_I i$ and $\tilde{v}_T^* = V_R - V_I i$ into Eq. (17) gives

$$\bar{U} = \frac{\pi V_I}{2\omega f}\left(k_f - k_e\right). \qquad (18)$$

Since $k_f > k_e$, the asymmetric tidal mixing over the M_2 tidal cycle produces an onbank net water flux on the southern flank.

Similar results can also be found on the northern flank. Since an onbank tidal flow on the southern flank corresponds to an offbank tidal flow on the northern flank, $k(t)$ can be expressed on the northern flank as

$$k(t) = \begin{cases} k_e \sin\omega t & 0 \le t \le \pi/\omega \\ -k_f \sin\omega t & \pi/\omega \le t \le 2\pi/\omega. \end{cases} \qquad (19)$$

Substituting Eq. (19) into Eq. (14) and conducting similar operations as above yields

$$\bar{U} = -\frac{\pi V_I}{2\omega f}\left(k_f - k_e\right). \qquad (20)$$

Since $k_f > k_e$, we can see that the asymmetric tidal mixing over the M_2 tidal cycle tends to produce an onbank net water flux on the northern flank.

This simple analytical model demonstrates that when

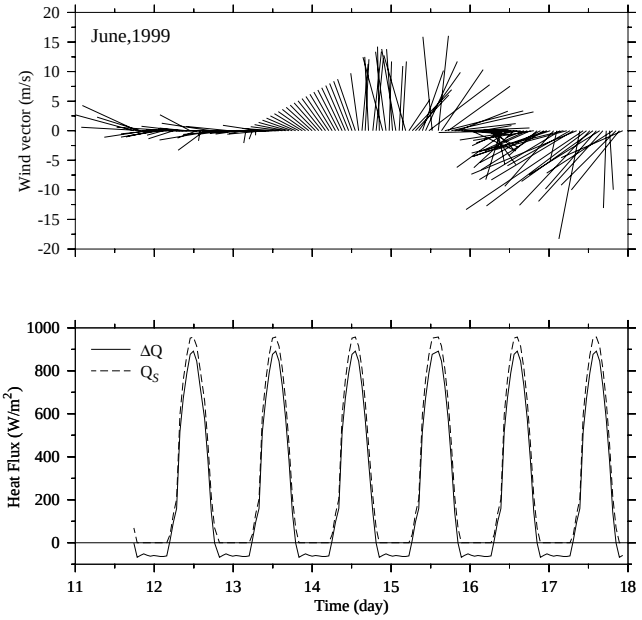

Fig. 13. Time series of the surface wind velocity vectors and heat flux on the southern flank of Georges Bank. The wind data was obtained from the June 1999 cruise around the tidal mixing front on the southern flank of the center Georges Bank, and the heat flux data came from the 1995 meteorological buoy measurement on the southern flank. ΔQ and Q_S are the net surface heat flux and shortwave radiation, respectively.

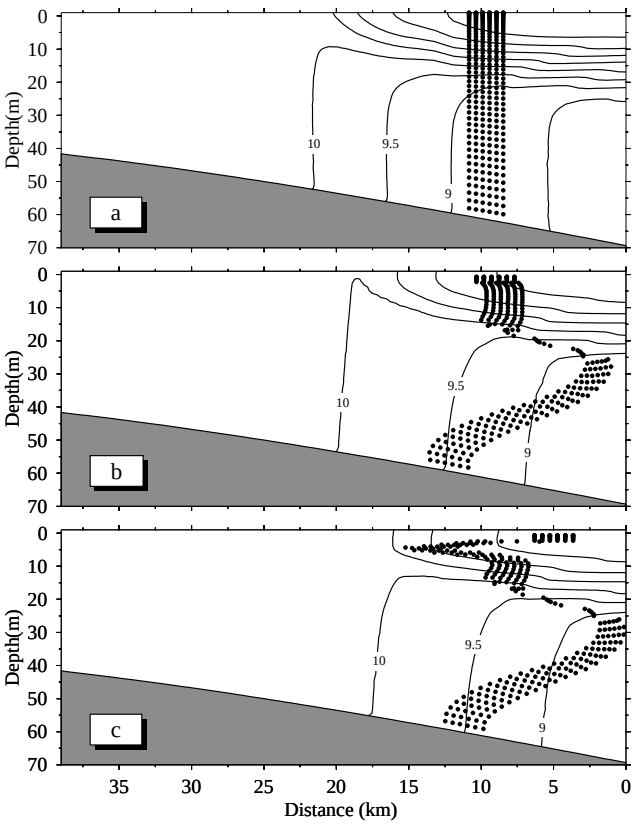

Fig. 14. Distribution of particles at the initial (the 11th model day) (upper) and at the 15.5th model day for the cases with tidal forcing only (middle) and with tidal forcing plus mean wind (lower). The contours are the model-predicted temperatures

tidal mixing is stronger during the on-bank (flood) tidal flow than during the off-bank (ebb) flow, it tends to produce an onbank net water flux from the stratified region to the mixed region around GB. This mixing-induced, onbank net water flux can play an important role in the summertime onbank, cross-frontal nutrient flux on GB. A comprehensive discussion of this subject was given in Pringle and Franks (2001), who used both 2D semi-analytical and numerical models to make quantitative estimates of the mixing-induced nutrient flux across the tidal mixing front on GB.

3.3 Time-varying wind stress

In a steady frontal system, the cross-frontal water transport is equal to the Ekman flux ($\tau/\rho_o f$), where τ is the along-frontal component of the surface wind stress. If a return flow is taken into account, the net cross-frontal flux should be smaller (Garrett and Loder, 1981). However, in the real world, the wind stress not only produces the Ekman transport but also causes the horizontal migration of the location of the front in the direction of Ekman transport. It is not clear how much cross-frontal water transport would occur in the case of wind forcing, and estimates of the net transport cannot be simply estimated using Ekman transport theory on the basis of the steady frontal dynamics.

Chen *et al*. (2001c) used a 2D numerical model to examine the role of the summertime wind stress in the cross-frontal water transport on the southern flank of GB. The model was initialized using the June 1999 hydrographic survey data with a well-defined TMF around the 50-m isobath and a sharp subsurface thermocline and thermohaline at about 10–25 m. The model was run first with tidal forcing only for 10 days. After the tidal currents and residual flow reached a quasi-equilibrium state, the wind stress and surface heat flux were added (Fig. 13). Fluid particles were released throughout the water column in the stratified region around the 60-m isobath at the beginning of the 11th model day (Fig. 14a), and then tracked for several M_2 tidal cycles under different physical forcing environments with tide only, tide plus averaged wind stress, tide plus realistic time-varying wind stress, and tide plus realistic wind and surface heat flux.

In the case with tide only, the model-predicted particle trajectories show that the water moves onbank in the

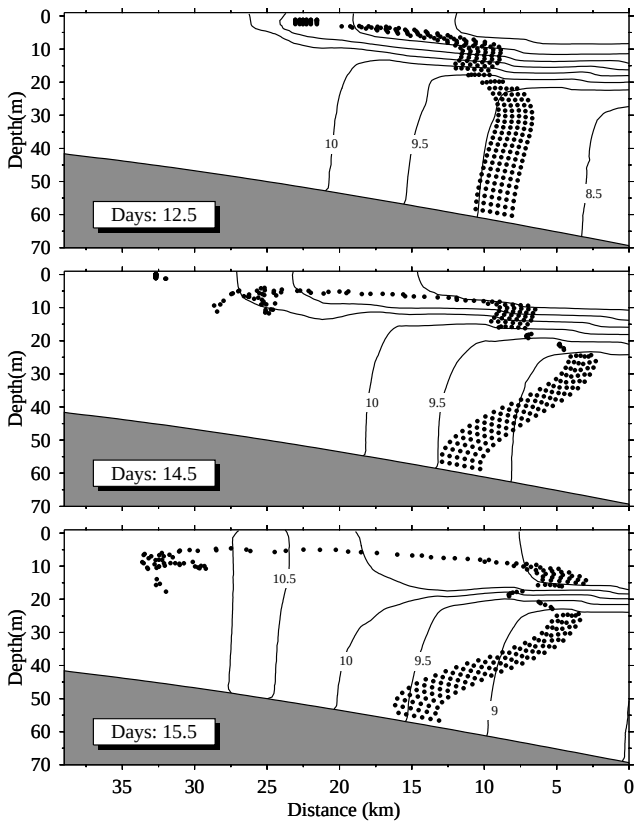

Fig. 15. Distribution of particles at the 12.5th (upper), 14.5th (middle), and 15.5th (lower) model days for the case with tidal forcing plus realistic wind. The contours are the model-predicted temperatures.

upper and lower mixed layer and offbank in the thermocline. This trajectory pattern is very similar to the cross-bank secondary circulation structure predicted by the semi-analytical, diagnostic frontal model shown in Section 2. No particles were found to cross the TMF over the time scale of a week (Fig. 14b). When a relatively weak mean wind stress of 0.023 N/m^2 directed towards 103.4° was added, the particles near the surface above 5 m exhibited more offbank movement due to the Ekman transport while deeper particles moved onbank as a result of the return flow. However, no significant cross-frontal exchange of particles occurred in this case over a period of 5 days (Fig. 14c).

In the case with tide plus realistic, time-varying wind stress, a significant onbank migration of the front occurred in the upper 10 m in the first three days due to a considerable, northward Ekman transport. Correspondingly, particles within the upper mixed layer were carried onbank along with the onbank frontal migration, but no particles crossed the front during that period. When the wind stress decreased and turned northward after June 14, the entire water column in the region shallower than 50 m was vertically mixed again. As a result, the particles, which previously were within the front, appeared in the mixed region on the top of the bank (Fig. 15). This process clearly shows that the appearance of particles in the mixed region is caused by combined wind-induced advection and tidal mixing. In other words, if no mixing exists, the particles should move along the front and no cross-frontal particle movement would occur. Since random mixing was not included explicitly in the particle tracking, particles in these experiments are just the fluid parcels that represent the center of mass of dissolved tracers or passive fish larvae (whose swimming can be ignored in comparison to the strong tidal currents). These experiments also imply the importance of time-dependent wind stress and mixing on cross-frontal water transport in summer on GB.

3.4 Cross-frontal transport due to chaotic mixing

In general, the cross-frontal secondary circulation is characterized by a pair of closed circulation cells, with convergence toward the front near the surface and bottom and divergence at a depth above the bottom mixed layer (Garrett and Loder, 1981). In the surface-bottom mixed front caused by strong tidal mixing over steep bottom topography (Chen *et al*., 1995a, 2001a) or river runoff (Chapman and Lentz, 1994), the cross-frontal secondary circulation may consist of double circulation cells with convergence towards the front at the bottom and divergence away from the front at the surface. As we mentioned before, the closed circulation cells usually act as a retention zone or a dynamic barrier to the cross-frontal transport of dissolved material or passive particles. When an extra periodic forcing is applied, however, the particle trajectories can become chaotic and cross-frontal exchange may occur (Oonishi and Kunishi, 1979; Zimmerman, 1986; Ridderinkhof and Zimmerman, 1992; Ridderinkhof and Loder, 1994).

The position of the TMF on GB exhibits an oscillatory variation due to the fortnightly or monthly variation in the strength of the tidal mixing (Loder and Greenberg, 1986; Chen *et al*., 1995b). Daily satellite SST images show that the tidal mixing thermal front moves back and forth with a fortnightly period over a scale of about 5 to 10 km (Chen *et al*., 1995b). This frontal oscillation may cause a nutrient flux into the frontal zone at a rate of

$$Q_M = \left(L_M / T_M\right) DC \tag{21}$$

where L_M is the fortnightly or monthly front's excursion, T_M is the fortnightly or monthly period, D is the pycnocline depth, and C is the nutrient concentration (see Loder and Platt, 1985, for derivation). For given C, D and T_M, the flux increases as L_M increases, while for given C, D and L_M, the flux should be controlled by the fort-

nightly oscillation.

On the other hand, the fortnightly migration of the frontal position might act as an extra forcing to cause chaotic transport across the frontal zone. This process can be examined using a simple semi-analytical model given by Chen (unpublished manuscript). The basic features of cross-frontal currents associated with the fortnightly tidal oscillation can be captured using a double-cell circulation with streamfunction given as

$$\psi = \psi_0 \sin\frac{\pi z}{h(x)} \sin\frac{\pi}{L}\left[x - x_0(t)\right], \tag{22}$$

where x and z are Cartesian coordinates, positive seaward and upward; ψ_0 is the magnitude of the streamfunction; L the horizontal scale of the circulation cell; and $h(x)$ the water depth. $x_0(t)$ denotes the periodic migration of the double-cell circulation pattern. The cells oscillate around its center position of x_c with a frequency ω_1 and an amplitude a_0, i.e.,

$$x_0(t) = x_c - a_0 \sin\omega_1 t. \tag{23}$$

Assuming that the fluid is incompressible and nondivergent, the horizontal and vertical velocities ($u = dx/dt$ and $w = dz/dt$) can be expressed using the streamfunction as

$$\frac{dx}{dt} = -\frac{\partial\psi}{\partial z} = -U_0 \cos\frac{\pi z}{h(x)} \sin\frac{\pi}{L}\left[x - x_0(t)\right] \tag{24}$$

$$\frac{dz}{dt} = \frac{\partial\psi}{\partial x} = W_0\left\{\sin\frac{\pi z}{h(x)}\cos\frac{\pi}{L}\left[x - x_0(t)\right] - \frac{L\alpha z}{h^2(x)}\cos\frac{\pi z}{h(x)}\sin\frac{\pi}{L}\left[x - x_0(t)\right]\right\} \tag{25}$$

where $U_0 = \psi_0\pi/H(x)$; $W_0 = \psi_0\pi/L$; and $\alpha = dh(x)/dx$. The phase portrait described by Eqs. (24) and (25) contains a stable "fixed" point at the surface and an unstable "fixed" point at the bottom at the inter-cell boundary. The bottom depth is specified as

$$h(x) = \begin{cases} H_0 & x < -L \\ 0.5\left(H_d + H_0\right) & \\ \quad -0.5\left(H_d - H_0\right)\cos\dfrac{\pi}{L_s}(x + L) & -L \le x < L_s - L \\ H_d & x \ge L_s - L \end{cases} \tag{26}$$

where H_0 = 40 m, H_d = 80 m, L_s = 30 km, and L was specified as 5 km.

Particle trajectories were calculated using the fourth-order Runge-Kutta method with a time step of 50 sec or less. Our study of cross-frontal exchange of particles focused on a double-cell frontal system with an oscillating inter-cell boundary at $x_0(t)$ and in a range of $-L - x_0(t) \le x \le L + x_0(t)$. Outside this range, the currents were specified as zero. In the numerical experiments, the double cells started oscillating around the origin of the x-axis, i.e., $x_c = 0$.

The numerical experiments were conducted for the case with a horizontal oscillation period of 14 days (a spring tidal cycle). Initially, a_0 was chosen as 2.5 km, and later some experiments with a variety of a_0 were made to examine the sensitivity of the cross-frontal chaotic transport to the horizontal migration scale of the front. The results obtained from these studies can be easily extended to the cases with monthly and seasonal variation scales.

An advection time scale T_{adv} was used as a reference time scale in this study. It was defined as an average time scale for particles to move around the closed streamlines at the outer edge of the cell, i.e.

$$T_{adv} = 2\left(\frac{L}{U_0} + \frac{H}{W_0}\right) = \frac{4H}{W_0}. \tag{27}$$

In the case with a steady front ($a_0 = 0$) and a given magnitude of the streamfunction $\psi_0 = 0.35$ m^2/s, all particles, which are released initially near the surface at the center of each circulation cell, travel exactly along the streamlines with an advective time scale of 8.4 days or less. No particles cross the inter-cell boundary during an integration period of 14 days or even much longer (Fig. 16a).

In the case with the same ψ_0 but a_0 = 2.5 km and the front moved back and forth with a period of 14 days, the trajectories of some particles became chaotic. In the right cell, two particles move across the instantaneous inter-cell boundary near the bottom close to the unstable "fixed" point between cells (Fig. 16b), even though most particles move counterclockwise and recirculated around the oscillatory trajectories. In the left cell, all ten particles move seaward and crossed the instantaneous inter-cell boundary during the first migration cycle. Although six of these particles turn clockwise and moved back to the left cell in the second cycle, four of them escaped and joined the right-cell circulation (Fig. 16c). The pattern of the inter-cell exchange of particles varies with the initial direction of the oscillation. When the front starts oscillating seaward first, the distribution of the inter-cell exchange of particles shown in Figs. 16b and 16c can be

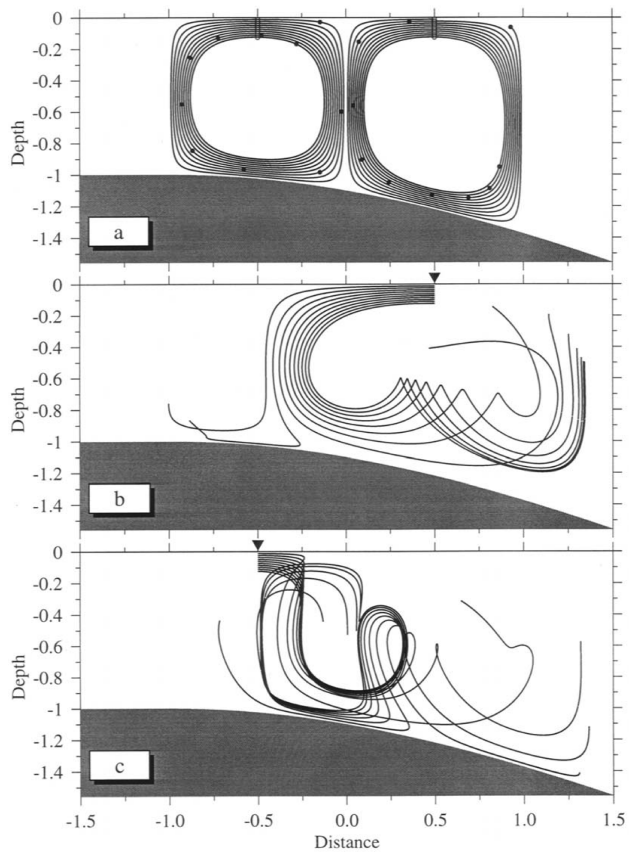

Fig. 16. Trajectories of 20 particles released near the surface at the center of the circulation cells for the cases in which the double cells were steady (a) and oscillated with a period of 14 days (b) and (c). In both the cases, ψ_0 = 0.35 m^2/s and L = 5 km. In the oscillatory case, a_0 = 2.5 km. The open circles and filled dots in (a) are the initial and ending positions of particles. The filled downtriangle in (b) and (c) indicates the starting location of particles. The cross-shelf distance and vertical depth were scaled by 5 km and 40 m.

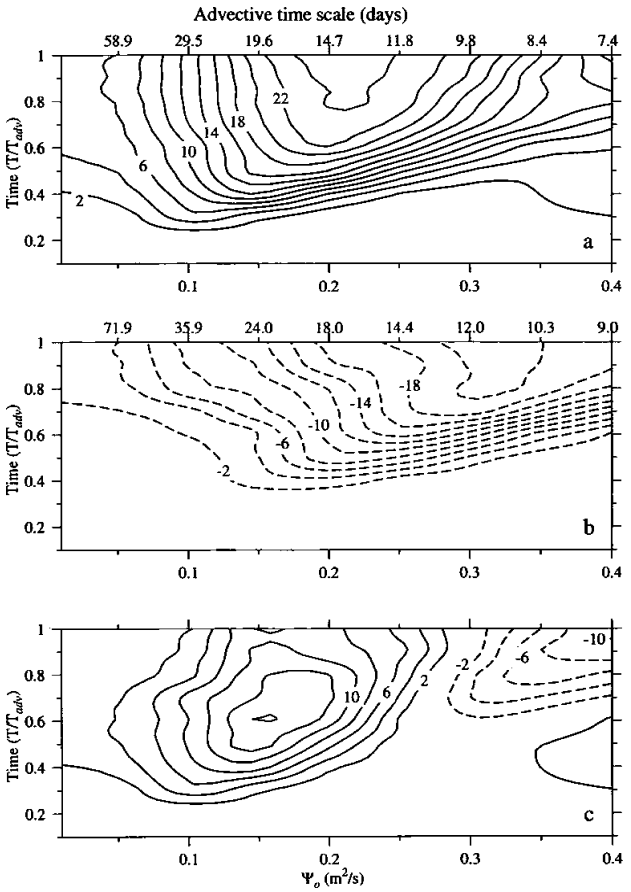

Fig. 17. The distribution of the percent of the cross-cell particles with respect to the amplitude of the cell circulation (ψ_0) and the non-dimensional time scaled by the advective time scale (T/T_{adv}) for the sloping-bottom case (a: seaward-from the left cell to the right cell; b: onshore-from the right cell to the left cell). The digital number at the top of (a) and (b) indicates the advective time scale (days) for a given ψ_0.

reversed.

The cross-cell chaotic transport appears to be closely related to the advective time scale T_{adv}. The transport of particles from the left cell to the right cell reached its maximum when T_{adv} is close to the period of the oscillating double cells (Fig. 17a). Such a transport decreases when T_{adv} is either increased or decreased. Similarly, the transport of particles from the right cell to the left cell has its maximum when T_{adv} is close to 11 days, and also decreases when T_{adv} is either increased or decreased (Fig. 17b). This asymmetric structure of cross-cell transport is still true in the case with a flat bottom, even though in this case the residual flow is the same in both right and left cells. The asymmetric pattern of the cells over the sloping bottom topography tends to produce a net cross-cell flux of particles. When T_{adv} is close to, or longer than, the oscillation period of the double cells, the flux is from left to right. Otherwise, the flux is from right to left (Fig. 17c).

The fact that the largest cross-cell chaotic transport of particles occurs when the advective time scale of the particles is close to the period of the oscillating front suggests that resonance may be an optimal condition to cause significant cross-front particle exchange in a deterministic vorticity-dominated flow field. A simple analytical approach is used here to explore the resonant nature of cross-cell chaotic transport in an oscillating frontal system. For simplification, the water depth is assumed to be constant, i.e., $h(x) = H_0$. A coordinate transformation is introduced of the form

$$\xi = \frac{W_0}{U_0}\left[x - x_0(t)\right] + z, \quad \eta = \frac{W_0}{U_0}\left[x - x_0(t)\right] - z. \quad (28)$$

Replacing x and z in Eqs. (24) and (25) by the transformation (28), yields

$$\frac{d\xi}{dt} = -W_0 \sin\frac{\pi}{H_0}\eta + \frac{W_0 a_0 \omega}{U_0}\cos\omega t \quad (29)$$

$$\frac{d\eta}{dt} = -W_0 \sin\frac{\pi}{H_0}\xi + \frac{W_0 a_0 \omega}{U_0}\cos\omega t. \quad (30)$$

Equations (29) and (30) are first-order nonlinear differential equations, in which the oscillation of the frontal position acts as an extra periodic forcing. Since the chaotic behavior of particles frequently occurs near the bottom close to the unstable "fixed" point between cells, we can simplify Eqs. (29) and (30) by searching for an asymptotic solution near the bottom.

Consider a phase plane near $\eta \to H_0$ and $\xi \to -H_0$ we can replace $\sin\pi\eta/H_0$ and $\sin\pi\xi/H_0$ by the approximate functions $\pi(\eta - H_0)/2H_0$ and $-\pi(\xi + H_0)/2H_0$, which leads to the following linear system

$$\frac{d\xi}{dt} = -\frac{\pi W_0}{2H_0}\left(\eta - H_0\right) + \frac{W_0 a_0 \omega}{U_0}\cos\omega t \quad (31)$$

$$\frac{d\eta}{dt} = \frac{\pi W_0}{2H_0}\left(\xi + H_0\right) + \frac{W_0 a_0 \omega}{U_0}\cos\omega t. \quad (32)$$

Eliminating η from Eqs. (31) and (32) results in the second-order wave equation

$$\frac{d^2\left(\xi + H_0\right)}{dt^2} + \frac{W_0\pi^2}{4H^2}\left(\xi + H_0\right) = -\frac{W_0}{U_0}a_0\omega^2 \sin\omega t - \frac{W_0^2 a_0 \omega\pi}{2H_0 U_0}\cos\omega t. \quad (33)$$

A particular solution for Eq. (33) is

$$\xi + H_0 = \frac{W_0 a_0 \omega}{U_0\left(\omega^2 - \frac{W_0^2\pi^2}{4H_0^2}\right)}\left(\omega \sin\omega t + \frac{W_0\pi}{2H_0}\cos\omega t\right). \quad (34)$$

The solution of Eq. (34) suggests that the oscillating frontal system may become resonant when

$$T_\omega = \frac{2\pi}{\omega} = \frac{4H_0}{W_0} = T_{\text{adv}}, \quad (35)$$

i.e., where the frontal oscillation period T_ω is equal to the particle advective time scale T_{adv}. Although this solution (35) only represents a special case of a linear oscillating frontal system, this solution is consistent with the numerical model results that show a significant cross-cell chaotic transport in the case when T_{adv} is close to T_ω. Therefore, the large chaotic cross-cell transport predicted in a fully nonlinear, double-cell oscillating frontal system may be the result of the chaotic process associated with resonance.

4. Some Critical Issues and a New Modeling Approach

To provide an accurate estimation of the cross-frontal water transport, one needs to have a model that conserves mass numerically. In general, however, mass conservation cannot be guaranteed for the discrete equations used in numerical simulation. This can be seen clearly in the example shown below.

Consider the following 1-D advective equation of a passive tracer

$$\frac{\partial C}{\partial t} + U\frac{\partial C}{\partial x} = 0 \quad (36)$$

where C is the tracer concentration and U is the x-component of the velocity. This equation can be solved numerically using a finite-difference scheme. For simplification, let us solve it using an upwind scheme as

$$C^{n+1} = C^n + U\frac{\Delta t}{\Delta x}\left(C_{i+1}^n - C_i^n\right) \quad (37)$$

where n is the n-th time step; i is the i-th grid point in the x direction, and Δt and Δx are the time step and spatial grid size, respectively. This discrete equation preserves the conservative tracer concentration only if

$$U\frac{\Delta t}{\Delta x} = 1 \quad \text{or} \quad \frac{\Delta x}{\Delta t} = U. \quad (38)$$

This indicates that the conservative law can be guaranteed only if the numerical advective velocity $\Delta x/\Delta t$ always is the same as the true advective velocity U. If U is constant, then this condition can be easily guaranteed by choosing Δx to Δt satisfy (38). However, U generally varies with time and space so that it is impossible to choose Δx and Δt in a way that condition (38) is always satisfied. This means that this numerical scheme in general does

not conserve the tracer, i.e., it is a damping scheme. Similar problems can be found in other finite-difference and finite-element approaches, especially in situations with sharp thermoclines or discontinuous flow at a front. This problem becomes worse in 3D models with the σ-coordinate transformation in the vertical (Chen and Liu, 2001). Therefore, we consider that the cross-frontal transport results previously obtained using finite-difference models are probably only qualitatively meaningful.

Recently, the finite-volume method has been received more and more attention in the numerical computation of fluid dynamics (Dick, 1994). Instead of the differential form, the finite-volume method discretizes the integral form of the equations, which is a better approach to ensure conservation of mass, momentum, and heat. Since these integral equations can be solved numerically by the flux calculation used in the finite-difference method over an arbitrary-size triangular mesh like those in the finite-element method, the finite-volume method, to a certain extent, combines the best of the finite-difference method for the simplest discrete computational efficiency and the a finite-element method for geometric flexibility.

For a 2D tracer equation, for example, the local change of the tracer concentration can be numerically integrated using the flux calculation as

$$\iint \frac{\partial C}{\partial t}\,dxdy = -\iint \left[\frac{\partial (UC)}{\partial x} + \frac{\partial (VC)}{\partial y}\right] dxdy = -\oint_{s'} V_n C ds' \quad (39)$$

where V_n is the velocity component normal to the sides of the triangle and s' is the closed path formed by the three sides. If Eq. (39) is integrated numerically using the same upwind scheme, it will have a second-order accuracy since the advective term has been expressed in the integral form of the flux. If a modified fourth-order Runge-Kutta time stepping scheme is adopted, it can significantly improve the accuracy of the advective term computation.

Chen *et al*. (2001d) have developed an unstructured grid finite-volume 3D primitive equation ocean model. The model consists of momentum, continuity, temperature, salinity and density equations and is closed physically and mathematically using the Mellor and Yamada level 2.5 turbulence closure submodel. The irregular bottom slope is represented using a σ-coordinate transformation and the horizontal grid is comprised of unstructured triangle cells. The currents, temperature and salinity in the model are computed using the integral form of the equations. Chen *et al*. (2001d) have applied this model to the Bohai Sea, a semi-enclosed coastal ocean, and the Satilla River, an estuary containing numerous tidal creeks and inlets. Compared with the results obtained from the finite-difference model (an updated version of the Princeton Ocean Circulation Model; called ECOM-si), this new model provides a better simulation of tidal elevations and residual currents, especially around islands and tidal creeks. This new model seems to be a good tool for the study of cross-frontal water transport and ecosystem dynamics where sharp gradients can be poorly resolved using finite-difference methods.

5. Summary

The recent progress in modeling cross-frontal exchange on Georges Bank has been reviewed and discussed. The discussion is focused on four physical mechanisms responsible for cross-frontal water transport on GB: (1) strong nonlinear interaction, (2) asymmetric tidal mixing, (3) time-varying wind forcing, and (4) chaotic mixing. Some critical issues in numerical modeling studies of the cross-frontal transport also are addressed. A new unstructured grid, finite-volume coastal ocean circulation model is introduced. This model combines the simple discrete computational efficiency that characterizes finite-difference methods and the geometric flexibility that characterizes finite-element methods. Because the finite-volume method discretizes the integral form of the equations, it is a better approach to conserve mass, momentum and heat, particularly in frontal regions where property gradients can be large.

It should be noted that this review covers only some of the modeling activities in the U.S. GLOBEC/Georges Bank Program phase III studies on the dynamics of the tidally mixed front (TMF). Several dye experiments were conducted on GB in 1999 to examine the cross-frontal water transport near the bottom on GB. These experiments have provided clear evidence of the cross-frontal flux of dye in the TMF on GB, which supports the model results discussed in this text (Houghton and Ho, 2001). Also, periodic surveys of the distribution of larval fish suggest that fish larvae are transported onbank across the TMF. Additional information and data can be obtained at the U.S. GLOBEC/Georges Bank Program web site, and in two special issues of Deep-Sea Research II that focus on results from the Georges Bank Program.

Acknowledgements

We thank guest editors of the Special Issue of Journal of Oceanography for inviting us to write a paper on the modeling efforts of the U.S. GLOBEC/Georges Bank Program. This research was conducted as part of the U.S. GLOBEC Georges Bank Program through support from NOAA grants NA56RG0487, NA96OP003, and NA96OP005 to Changsheng Chen and NSF grant OCE98-06379 to Robert Beardsley. U.S. GLOBEC contribution number is 193.

References

Butman, B., R. C. Beardsley, B. Magnell, D. Frye, J. A. Vermersch, R. Schlitz, R. Limeburner, W. R. Wright and M. A. Noble (1982): Recent observations of the mean circulation on Georges Bank. *J. Phys. Oceanogr*., **12**, 569–591.

Chapman, D. C. and S. J. Lentz (1994): Trapping of a coastal density front by the bottom boundary layer. *J. Phys. Oceanogr*., **24**, 1464–1479.

Chen, C. and R. C. Beardsley (1995): Numerical study of stratified tidal rectification over finite-amplitude banks. Part I: symmetric banks. *J. Phys. Oceanogr*., **25**, 2090–2110.

Chen, C. and R. C. Beardsley (1998): Tidal mixing and cross-frontal particle exchange over a finite amplitude asymmetric bank: a model study with application to Georges Bank. *J. Mar. Res*., **56**, 1165–1201.

Chen, C., R. C. Beardsley and R. Limeburner (1995a): Numerical study of stratified tidal rectification over finite-amplitude banks. Part II: Georges Bank. *J. Phys. Oceanogr*., **25**, 2111–2128.

Chen, C., R. C. Beardsley and R. Limeburner (1995b): Variability of water properties in late spring in the northern Great South Channel. *Cont. Shelf Res*., **15**, 415–431.

Chen, C., R. Beardsley and P. J. S. Franks (2001a): A 3-D prognostic numerical model study of the Georges Bank ecosystem. Part I: physical model. *Deep-Sea Res. II*, **48**(1–3), 419–456.

Chen, C., Q. Xu, R. Beardsley and P. J. S. Franks (2001b): Model study of the cross-frontal water exchange on Georges Bank: a 3-D Lagrangian experiment. *J. Geophys. Res*. (accepted).

Chen, C., R. Schlitz, R. Beardsley, K. Smith, J. P. Manning and G. Lough (2001c): Wind-induced, cross-frontal water exchange on Georges Bank: A mechanism for the early summer on-bank larval transport (in preparation).

Chen, C., H. Liu and R. C. Beardsley (2001d): An unstructured grid, finite-volume, three-dimensional, primitive equations ocean model: Application to coastal ocean and estuaries. *J. Atmos. Ocean.Technol*. (in revision).

Dick, E. (1994): Introduction to finite-volume techniques in computational fluid dynamics. p. 271–297. In *Computational Fluid Dynamics*, ed. by J. F. Wendt, Springer.

Flagg, C. N. (1987): Hydrographic structure and variability. p. 108–124. In *Georges Bank*, ed. by R. H. Backus, The MIT Press.

Franks, P. J. S. and C. Chen (1996): Plankton production in tidal fronts: a model of Georges Bank in summer. *J. Mar. Res*., **54**, 631–651.

Franks, P. J. S. and C. Chen (2001): A 3-D prognostic numerical model study of the Georges Bank ecosystem. Part II: biological-physical model. *Deep-Sea Res. II*, **48**(1–3), 457–482.

Garrett, C. J. R. and J. W. Loder (1981): Dynamical aspects of shallow sea fronts. *Phil. Trans. R. Soc. Lond*., **A302**, 563–581.

Greenberg, D. A. (1983): Modeling the mean barotropic circulation in the Bay of Fundy and Gulf of Maine. *J. Phys. Oceanogr*., **13**, 886–904.

Horne, E. P. W., J. W. Loder, W. G. Harrison, R. Mohn, M. R. Lewis, B. Irwin and T. Platt (1989): Nitrate supply and demand at the Georges Bank tidal front. *Scient. Mar*., **53**, 145–158.

Houghton, R. W. and C. Ho (2001): Diapycnal flow through the Georges Bank tidal front: A dye tracer study. *Geophys. Res. Lett*. (submitted).

Limeburner, R. and R. C. Beardsley (1996): Near-surface recirculation over Georges Bank. *Deep-Sea Res. II*, **43**(7–8), 1547–1574.

Loder, J. W. (1980): Topographic rectification of tidal currents on the sides of Georges Bank. *J. Phys. Oceanogr*., **10**, 1399–1416.

Loder, J. W. and D. A. Greenberg (1986): Predicted positions of tidal fronts in the Gulf of Maine region. *Cont. Shelf Res*., **6**, 397–414.

Loder, J. W. and T. Platt (1985): Physical control on phytoplankton production at tidal fronts. p. 3–22. In *Proceedings of 19th European Marine Biology Symposium*, ed. by P. G. Gibbs, Cambridge University Press, Cambridge.

Loder, J. W. and D. G. Wright (1985): Tidal rectification and front circulation on the sides of Georges Bank. *J. Mar. Res*., **43**, 581–604.

Loder, J. W., Y. Shen and H. Ridderinkhof (1997): Characterization of three-dimensional Lagrangian circulation associated with tidal rectification over a submarine bank. *J. Phys. Oceanogr*., **27**, 1729–1742.

Lough, R. G. (1984): Larval fish trophodynamic studies on Georges Bank: sampling strategy and initial results. In *The Propoagation of cod Gadhus morhua L.*, ed. by E. Dahl, D. S. Danielssen, E. Moksness and P. Solemdal, Flodevingen rapporster 1, 395–434.

Lough, R. G. and J. P. Manning (2001): Tidal-front entrainment and retention of fish larvae on the southern flank of Georges Bank. *Deep-Sea Res. II*, **48**(1–3), 631–644.

Lough, R. G. and D. G. Mountain (1996): Effect of small-scale turbulence on feeding rates of larval cod and haddock in stratified waters on Georges Bank. *Deep-Sea Res. II*, **43**, 1745–1772.

Lough, R. G., G. R. Bolz, M. Pennington and M. D. Grosslein (1985): Larval abundance and mortality of Atlantic herring (*Clupea harengus L.*) spawned in the Georges Bank and Nantucket Shoals areas, 1971–78 seasons. In relation to spawning stock size. *J. Northw. Fish. Sci*., **6**, 21–35.

Moody, J. A., B. Butman, R. C. Beardsley, W. S. Brown, P. Daifuku, J. D. Irish, D. A. Mayer, H. O. Mofjelf, B. Petrie, S. Ramp, P. Smith and W. R. Wright (1984): *Atlas of Tidal Elevation and Current Observations on the Northeast American Continental Shelf and Slope*. U.S. Geological Survey Bulletin 1611, 122 pp.

Mountain, D. G. and M. H. Taylor (1996): Fluorescence structure in the region of the tidal mixing front on the southern flank of Georges Bank. *Deep-Sea Res. II*, **43**, 1831–1854.

Oonishi, Y. and H. Kunishi (1979): Water exchange between adjacent vortices under an additional oscillatory flow. *J. Oceanogr. Soc. Japan*, **35**, 136–140.

O'Reilly, J. E., C. Evans-Zetlin and D. A. Busch (1987): Primary production. p 220–233. In *Georges Bank*, ed. by R. H. Backus, The MIT Press, Cambridge, MA.

Pingree, R. D. (1979): Baroclinic eddies bordering the Celtic

Sea in late summer. *J. Mar. Biol. Ass. U.K.*, **54**, 689–698.
Pringle, J. M. and P. J. S. Franks (2001): Asymmetric mixing transport: a horizontal transport mechanism for sinking plankton and sediment in tidal flows. *Limnol. Oceanogr.*, **46**(2), 381–391.
Ridderinkhof, H. and J. W. Loder (1994): Lagrangian characterization of circulation over submarine banks with application to the outer Gulf of Maine. *J. Phys. Oceanogr.*, **24**, 1184–1200.
Ridderinkhof, H. and J. T. F. Zimmerman (1992): Chaotic stirring in a tidal system. *Science*, **258**, 1107–1111.
Riley, G. A. (1941): Plankton studies. IV. Georges Bank. *Bull. Binghampton Oceanogr. Coll.*, **7**, 1–73.
Smith, W. and W. W. Morse (1985): Retention of larval haddock *Melanogrammus aeglefinus* in the Georges Bank region, a gyre-influenced spawning area. *Mar. Ecol. Prog. Ser.*, **24**, 1–13.
Townsend, D. W. and N. R. Pettigrew (1996): The role of frontal currents in larval fish transport on Georges Bank. *Deep-Sea Res. II*, **43**, 1773–1792.
U.S. GLOBEC (1992): Northwest Atlantic Implementation Plan. Rept. No. 6.
Wiebe, P. H. and R. Beardsley (1996): Physical-biological interactions on Georges Bank and its environs. *Deep-Sea Res. II*, **43**, 1437–1438.
Zimmerman, J. T. F. (1978): Topographic generation of residual circulation by oscillatory tidal currents. *Geophys. Astr. Fluid Dyn.*, **11**, 35–47.
Zimmerman, J. T. F. (1980): Vorticity transfer by tidal currents over an irregular topography. *J. Mar. Res.*, **38**, 601–630.
Zimmerman, J. T. F. (1986): The tidal whirlpool: a review of horizontal dispersion by tidal and residual currents. *Netherlands Journal of Sea Research*, **20**(2/3), 133–154.